

# Dynamic wetting failure and hydrodynamic assist in curtain coating

Chen-Yu Liu<sup>1</sup>, Eric Vandre<sup>1</sup>, Marcio S. Carvalho<sup>2,†</sup> and Satish Kumar<sup>1,†</sup>

<sup>1</sup>Department of Chemical Engineering and Materials Science, University of Minnesota, Minneapolis, MN 55455, USA

<sup>2</sup>Department of Mechanical Engineering, Pontificia Universidade Católica do Rio de Janeiro, Rio de Janeiro, RJ, 22451-900, Brazil

(Received 8 March 2016; revised 10 August 2016; accepted 5 September 2016; first published online 28 October 2016)

Dynamic wetting failure in curtain coating of Newtonian liquids is studied in this work. A hydrodynamic model accounting for air flow near the dynamic contact line (DCL) is developed to describe two-dimensional (2D) steady wetting and to predict the onset of wetting failure. A hybrid approach is used where air is described by a one-dimensional model and liquid by a 2D model, and the resulting hybrid formulation is solved with the Galerkin finite element method. The results reveal that the delay of wetting failure in curtain coating – often termed hydrodynamic assist – mainly arises from the hydrodynamic pressure generated by the inertia of the impinging curtain. This pressure leads to a strong capillary-stress gradient that pumps air away from the DCL and thus increases the critical substrate speed for wetting failure. Although the parameter values used in the model are different from those in experiments due to computational limitations, the model is able to capture the experimentally observed non-monotonic behaviour of the critical substrate speed as the feed flow rate increases (Blake *et al.*, *Phys. Fluids*, vol. 11, 1999, p. 1995–2007). The influence of insoluble surfactants is also investigated, and the results show that Marangoni stresses tend to thin the air film and increase air-pressure gradients near the DCL, thereby promoting the onset of wetting failure. In addition, Marangoni stresses reduce the degree of hydrodynamic assist in curtain coating, suggesting a possible mechanism for experimental observations reported by Marston *et al.* (*Exp. Fluids*, vol. 46, 2009, pp. 549–558).

**Key words:** coating, contact lines, interfacial flows (free surface)

## 1. Introduction

Dynamic wetting is a common phenomenon in everyday life and industrial coating operations where an ambient fluid (often air) is displaced by a liquid on a solid surface. In particular, coating flows rely heavily on steady dynamic wetting to uniformly deposit a liquid on a moving substrate (Weinstein & Ruschak 2004). Dynamic wetting fails at some critical substrate speed and is accompanied by a change in flow from steady two-dimensional (2D) to unsteady three-dimensional (3D)

† Email addresses for correspondence: [msc@puc-rio.br](mailto:msc@puc-rio.br), [kumar030@umn.edu](mailto:kumar030@umn.edu)

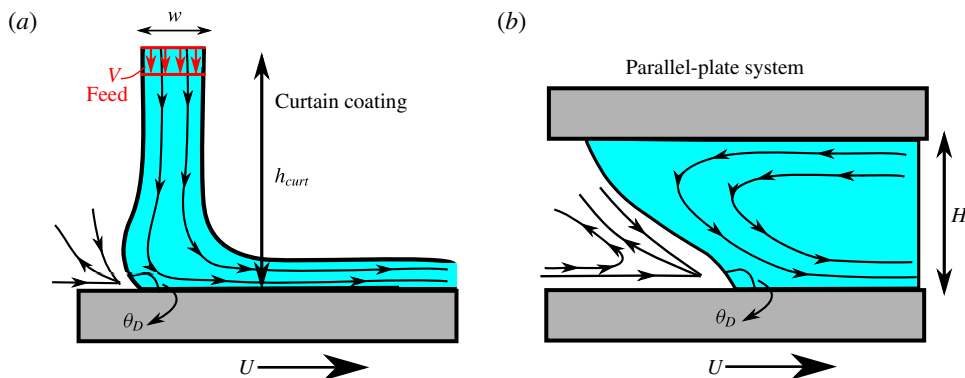


FIGURE 1. (Colour online) Schematics of (a) curtain coating and (b) parallel-plate geometry.

flow (Burley & Kennedy 1976; Blake & Ruschak 1979; Vandre, Carvalho & Kumar 2014). In coating processes, wetting failure leads to air entrainment and can degrade product quality (Kistler 1993; Weinstein & Ruschak 2004). Therefore, understanding the mechanisms of wetting failure is very important so that strategies to delay the onset of wetting failure and increase coating speed can be developed.

Curtain coating is a high-speed coating method where substrate speeds of  $U \approx 10 \text{ m s}^{-1}$  can be achieved (Brown 1961; Hughes 1970; Blake *et al.* 1995; Blake, Dobson & Ruschak 2004). In this method, liquid is extruded (at a feed flow velocity  $V$ ) from a die (of width  $w$ ) at a height  $h_{\text{curt}}$  onto a moving substrate (figure 1a). Gravity accelerates the liquid as it flows down the curtain (Kistler 1985; Blake, Clarke & Ruschak 1994). A uniform film of thickness  $h_{\text{inf}}$  is formed on the substrate when the liquid flow is steady and 2D. The ability to achieve high substrate speeds has made curtain coating a popular mass production method (Miyamoto & Katagiri 1997). However, the mechanism of wetting failure in curtain coating remains poorly understood.

### 1.1. Hydrodynamic assist

The term ‘hydrodynamic assist’ is used to describe the fact that curtain coating can be manipulated to assist dynamic wetting and delay the onset of wetting failure (i.e. air entrainment) (Blake *et al.* 1994; Miyamoto & Katagiri 1997). It was found that manipulating the feed flow velocity  $V$  in curtain coating can postpone the onset of wetting failure to a higher critical substrate speed  $U^{\text{crit}}$  in comparison with ‘plunge coating’, where a solid substrate plunges into a liquid pool (Blake, Bracke & Shikhmurzaev 1999; Yamamura 2007). Experimental observations show that the degree of hydrodynamic assist reaches its maximum (i.e. the largest critical speed) when the dynamic contact line (DCL) is right beneath the liquid curtain, which leads to a strong hydrodynamic pressure near the DCL as the liquid impacts the substrate (Blake *et al.* 1994; Miyamoto & Katagiri 1997; Blake *et al.* 1999; Yamamura *et al.* 2000; Blake *et al.* 2004; Yamamura 2007).

Flow visualizations near the DCL show that manipulating  $V$  (at a given substrate speed  $U$ ) can also lead to a reduction in the dynamic contact angle  $\theta_D$ , the observed angle between the fluid interface and the substrate at the DCL (figure 1a) (Blake *et al.* 1999, 2004; Clarke & Stattersfield 2006; Decent 2008). To study the origin of

the reduction in  $\theta_D$ , Wilson *et al.* (2001, 2006) developed a hydrodynamic model for curtain coating with a fixed microscopic contact angle  $\theta_{mic}$  prescribed at the DCL. Note that  $\theta_{mic}$  serves as a boundary condition at the DCL and influences the free-surface shape (Blake 2006; Snoeijer & Andreotti 2013).

Their model prediction (Wilson *et al.* 2001, 2006) shows that the reduction in the apparent contact angle (i.e. interface angle calculated 20  $\mu\text{m}$  away from the DCL in their model and assumed to be equal to  $\theta_D$ ) is much smaller than the reduction in  $\theta_D$  observed experimentally by Blake *et al.* (1999). Therefore, Wilson *et al.* (2001, 2006) claimed that  $\theta_{mic}$  is not a constant and must depend on parameters controlling the overall flow (e.g. curtain height  $h_{curr}$  and feed flow rate  $Q = wV$ ). However, their hydrodynamic model does not consider the contribution of air stresses and, as a consequence, cannot predict a critical speed for wetting failure. As we will discuss below, air stresses are essential for determining the shape of the fluid interface and predicting wetting failure (Chan *et al.* 2013; Vandre, Carvalho & Kumar 2013; Vandre *et al.* 2014).

Before proceeding, we note that there are several different ways to describe dynamic wetting phenomena (Blake 2006; Snoeijer & Andreotti 2013; Sui, Ding & Spelt 2014; Blake *et al.* 2015). The first (and simplest) is to assume that  $\theta_{mic}$  is constant, and that all variations in  $\theta_D$  are due to bending of the fluid interface by viscous forces. The second is to assume that  $\theta_{mic}$  depends on substrate speed through a relationship like that obtained from the molecular kinetic theory of wetting. The third is to assume that  $\theta_{mic}$  depends on parameters controlling the overall flow, which is the approach of the interface formation model. Wilson *et al.* (2001, 2006) used the first approach and concluded that it cannot adequately describe the experimental observations. The conclusion of the present paper is that the first approach may be sufficient provided that air stresses are accounted for.

### 1.2. The role of air stresses

A common approach in previous computational studies of coating flows is to neglect the contribution of air stresses due to the low air viscosity (Kistler & Scriven 1984; Christodoulou & Scriven 1989; Wilson *et al.* 2001, 2006; Nam & Carvalho 2009). However, in our previous work on fluid displacement between two parallel plates (figure 1*b*), we have shown the need to incorporate the air phase to accurately describe the displacement process and predict wetting failure (Vandre, Carvalho & Kumar 2012; Vandre 2013; Vandre *et al.* 2013, 2014).

If air stresses are neglected in the model, 2D steady-state solutions can be obtained at any substrate speed, meaning that the onset of wetting failure (i.e. the critical substrate speed  $U^{crit}$ ) is completely missed (Vandre *et al.* 2013). By including the air-phase contribution to stress balances along the fluid interface, a limit point arises in the steady-state solution path ( $\theta_D$  versus  $U$ ), indicating that 2D steady solutions do not exist beyond a critical substrate speed. This critical speed marks the onset of wetting failure (Vandre *et al.* 2013). A stress-gradient analysis revealed that wetting failure occurs when capillary-stress gradients generated by interfacial curvature can no longer provide the pressure gradients needed to pump air away from the DCL, a mechanism supported by experimental studies (Vandre *et al.* 2013, 2014).

Notably, the geometry of curtain coating is significantly different from that of the parallel-plate system (figure 1). In the former geometry, liquid is fed from a coating die and creates two free surfaces (i.e. upstream and downstream fluid interfaces) as the liquid impacts the substrate. In the latter geometry, there is no feed flow and

only one free surface between two plates. However, even though these two geometries are very different, they both feature a thin air layer (wedge) near the DCL during fluid displacement, especially near the onset of wetting failure. Therefore, our previous work on the parallel-plate system (Vandre *et al.* 2013, 2014) suggests that it will be important to consider the contribution of air stresses when modeling curtain coating.

### 1.3. Influence of surfactants

Surfactants are known to lower the surface tension  $\sigma$ , and can also lower the static contact angle  $\theta_s$ , according to Young's equation (Tricot 1997). In addition, gradients in surfactant concentration can induce surface-tension gradients (i.e. Marangoni stresses), driving liquid from regions of low to high surface tension (Scriven & Sterling 1960). Experimental results reported by Marston *et al.* (2009) show that the addition of surfactant (sodium dodecyl sulphate) to glycerol/water mixtures significantly decreases the critical substrate speed  $U^{crit}$  (up to 66.7%) in curtain coating. In addition, the shape of the coating window (i.e. the parameter space within which the coating flow is steady and free of defects) is considerably modified, with the degree of hydrodynamic assist being greatly reduced by surfactants.

Marston *et al.* (2009) reported that, after the addition of surfactant, a twofold reduction in surface tension is observed but the liquid viscosity remains approximately the same. Since no non-Newtonian rheological behaviour is observed in the surfactant solutions, the change in the critical speed and the shape of the coating window suggests that surface-tension gradients (i.e. Marangoni stresses) may also play an important role. Our previous work with the parallel-plate system (figure 1*b*) demonstrates that the presence of Marangoni stresses promotes the onset of wetting failure (i.e. decreases  $U^{crit}$ ) by thinning the air film between the fluid interface and the substrate (Liu *et al.* 2016). However, since the geometries of the parallel-plate system and curtain coating are significantly different, it is not obvious that the physical mechanisms relevant to the parallel-plate system still hold in curtain coating.

### 1.4. Overview of present paper

In this paper, a hydrodynamic model for curtain coating accounting for the receding air flow is developed. Since a full 2D description of both the liquid and air phases is computationally prohibitive, here we use a less computationally intense approach that combines a 2D description of the liquid and a one-dimensional (1D) description of the air near the DCL. The 1D description is motivated by the observation of a long and slender air film as the interface deforms near the onset of wetting failure (Kistler 1993; Marchand *et al.* 2012; Vandre *et al.* 2014). This hybrid approach was used in our previous work (Liu *et al.* 2016) on the parallel-plate system (figure 1*b*) and its predictions were shown to be in excellent agreement with those from calculations using full 2D descriptions of both the air and liquid phases. Here, the hybrid approach is applied to a considerably more complicated geometry (figure 1*a*).

We solve this hybrid formulation of the hydrodynamic model with the Galerkin finite element method. By tracing steady-state solutions of the model as substrate speed increases, we can locate a critical substrate speed  $U^{crit}$  beyond which 2D steady solutions do not exist. This critical condition corresponds to the onset of wetting failure and is characterized by a critical capillary number  $Ca^{crit} = \mu_{adv} U^{crit} / \sigma$ , where  $\mu_{adv}$  is the viscosity of the advancing liquid and  $\sigma$  is the surface tension. Prior literature shows that the value of  $Ca^{crit}$  depends on various factors such as fluid properties (Marston, Simmons & Decent 2007; Marchand *et al.* 2012; Sprittles 2015), substrate properties (Benkreira 2004; Vandre *et al.* 2013) and flow geometry (Blake *et al.* 1999; Clarke & Stattersfield 2006; Vandre *et al.* 2012, 2014).

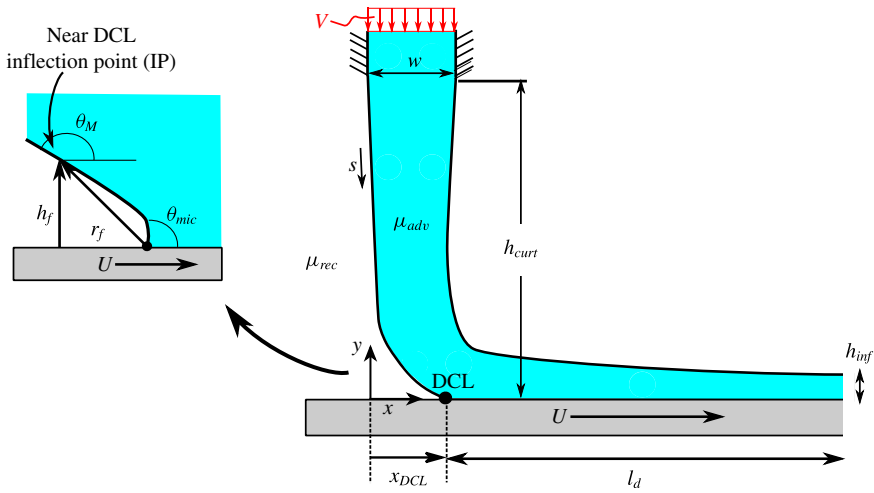


FIGURE 2. (Colour online) Schematic of physical coating domain and illustration of interface characteristics near the DCL. The IP corresponds to the maximum interface angle, and its height and radial distance are characterized by  $h_f$  and  $r_f$ , respectively.

The objective of the present paper is to determine how  $Ca^{crit}$  in curtain coating changes with the viscosity of the receding air  $\mu_{rec}$  (i.e. the strength of air stresses), feed flow rate  $Q$  (i.e.  $V$ ) and Marangoni stresses induced by surface-tension gradients. To examine how well the hydrodynamic model performs, we also compare our predictions of contact-angle behaviour with prior computational work by Wilson *et al.* (2001, 2006) and experimental work by Blake *et al.* (1999). In addition, physical explanations of hydrodynamic assist and Marangoni effects on wetting failure are proposed using a stress-gradient analysis (Vandre *et al.* 2013; Liu *et al.* 2016).

The mathematical formulation and solution method we use are described in § 2. In § 3, we discuss the influence of the receding phase and compare  $Ca^{crit}$  in curtain coating and the parallel-plate system. Hydrodynamic assist in curtain coating and its physical mechanism are examined in § 4. The variation of contact angle with feed flow rate is the topic of § 5. Section 6 presents results on the influence of surfactants on wetting failure and the underlying physical mechanisms. Finally, a summary of our results is provided in § 7.

## 2. Hydrodynamic model

In curtain coating, liquid is fed from an elevated slot die (width  $w$  and height  $h_{curt}$ ) with an average downward feed flow velocity  $V$  onto a substrate moving at speed  $U$  (figure 2). The liquid impacts the substrate at the DCL, whose position  $x_{DCL}$  depends on the problem parameters. The viscosities of the advancing (liquid) and the receding (air) fluids are denoted by  $\mu_{adv}$  and  $\mu_{rec}$ , respectively. The liquid density and surface tension are denoted by  $\rho$  and  $\sigma$ . Symbols  $x$  and  $y$  represent the Cartesian coordinates, whose origin is right beneath the upstream tip of the slot die as indicated in figure 2. During steady wetting, a coating film with a uniform thickness  $h_{inf} = Q/U$  is formed over the moving substrate, where  $Q = wV$  is the liquid flow rate per unit width from the slot die. Note that the domain length  $l_d$  extends to approximately  $5h_{curt}$  downstream to obtain a well-developed flow in the coating film.

The schematic of the region near the DCL (figure 2) shows the difference between the microscopic contact angle  $\theta_{mic}$  and the macroscopic contact angle  $\theta_M$ . The former angle ( $\theta_{mic}$ ) is located at the place where the interface contacts the substrate and serves as a boundary condition in our model. In contrast, the latter one ( $\theta_M$ ) is defined to be the maximum angle along the fluid interface and corresponds to the inflection point (IP) of the fluid interface. Note that  $\theta_M$  does not necessarily equal the dynamic contact angle  $\theta_D$ , the experimentally observed angle between the fluid interface and the substrate. The height of the IP and the radial distance from the DCL are denoted by  $h_f$  and  $r_f$ , respectively.

Since we are interested in the influence of Marangoni stresses on wetting failure, we will also consider the case where insoluble surfactants are present on the upstream fluid interface. We neglect the effect of surfactants on the downstream fluid interface because wetting failure occurs at the DCL.

### 2.1. Governing equations

The steady Navier–Stokes equations describe the velocity  $\mathbf{v}$  and pressure  $p$  in the liquid phase:

$$\nabla \cdot \mathbf{v} = 0, \quad Re(\mathbf{v} \cdot \nabla \mathbf{v}) = \nabla^2 \mathbf{v} - \nabla p + (Bo/Ca)\mathbf{g}. \tag{2.1a,b}$$

The lengths, velocities and stresses are non-dimensionalized with the characteristic scales  $Q/U$ ,  $U$  and  $\mu_{adv}U^2/Q$ , respectively. The Reynolds, capillary and Bond numbers are given by  $Re = \rho Vw/\mu_{adv}$ ,  $Ca = \mu_{adv}U/\sigma$  and  $Bo = (\rho g/\sigma)(wV/U)^2$ , respectively. The gravitational acceleration is given by  $\mathbf{g} = -g\mathbf{e}_y$ , where  $\mathbf{e}_y$  is the unit vector in the  $y$ -direction.

Near the DCL, the air phase is long and slender. Lubrication theory is thus applied to the air phase, resulting in a 1D description of the air flow (as described in our previous work (Vandre 2013; Liu *et al.* 2016)):

$$Ah + \frac{1}{2}Bh^2 + \frac{1}{6}\frac{dp}{ds}h^3 = 0, \tag{2.2}$$

$$\left. \frac{\partial u}{\partial y} \right|_s = B + \frac{dp}{ds}h \quad \text{where } A = \frac{\chi h + \chi \lambda u_s - \frac{1}{2}(dp/ds)h^2 \lambda}{\lambda + h}, \quad B = \frac{-\chi + A}{\lambda}, \tag{2.3}$$

where  $h$  is the interface height,  $p$  is the air pressure,  $u_s$  represents the horizontal interface velocity,  $\lambda = l_{slip}U/Q = l_{slip}/h_{inf}$  is a dimensionless slip length with  $l_{slip}$  being the dimensional slip length, and  $\chi = \mu_{rec}/\mu_{adv}$  is the viscosity ratio. The velocity gradient in (2.3) is evaluated at the interface. Note that the quasi-parallel (QP) approximation ( $dx \approx ds$ ) is used in (2.2) and (2.3) to express pressure gradients with respect to the arclength coordinate  $s$  along the interface (figure 2) (Jacqmin 2004; Sbragaglia, Sugiyama & Biferale 2008).

The following set of dimensionless boundary conditions is applied along the upstream fluid interface:

$$\mathbf{v}|_{rec} = \mathbf{v}|_{adv}, \tag{2.4}$$

$$\mathbf{n} \cdot \mathbf{v} = 0, \tag{2.5}$$

$$M \nabla_s \sigma \cdot \mathbf{t} = \mathbf{n} \cdot \mathbf{T} \cdot \mathbf{t}|_{adv} - \mathbf{n} \cdot \mathbf{T} \cdot \mathbf{t}|_{rec}, \tag{2.6}$$

$$\kappa(1/Ca + \sigma M) = \mathbf{n} \cdot \mathbf{T} \cdot \mathbf{n}|_{adv} - \mathbf{n} \cdot \mathbf{T} \cdot \mathbf{n}|_{rec}. \tag{2.7}$$

Equations (2.4) and (2.5) represent the no-slip and no-penetration boundary conditions, and (2.6) and (2.7) are interfacial stress balances. At the fluid interface,  $\mathbf{n}$  is the unit outward vector normal to the interface, and unit tangent vector  $\mathbf{t}$  points in the direction of increasing distance  $s$  along the interface (figure 2). Subscripts ‘adv’ and ‘rec’ indicate properties in the advancing and receding phases, respectively.

In the stress balances,  $\nabla_s \sigma$  denotes the surface-tension gradient along the interface,  $\kappa$  represents the interface curvature, and  $\mathbf{T}$  is the Newtonian stress tensor. The Marangoni and capillary numbers are defined as  $M = (\sigma_o - \sigma_m)/\mu_{adv}U$  and  $Ca = \mu_{adv}U/\sigma_m$ . Here,  $\sigma_o$  is the surface tension of the surfactant-free solution and  $\sigma_m$  is the surface tension corresponding to the mean surfactant concentration  $\Gamma_m$  at the interface. In the absence of surfactant,  $\sigma_o = \sigma_m$  and the Marangoni stresses vanish (i.e.  $M = 0$ ).

At the downstream fluid interface, the no-slip and kinematic boundary conditions (2.4) and (2.5) are still valid. However, since the air flow near the downstream interface is not expected to have significant effects on wetting failure, the stress contribution from the air phase there is neglected. The stress balances at the downstream interface become:

$$\mathbf{n} \cdot \mathbf{T} \cdot \mathbf{t}|_{adv} = 0, \quad (2.8)$$

$$\kappa = Ca(\mathbf{n} \cdot \mathbf{T} \cdot \mathbf{n}|_{adv} + P_{amb}), \quad (2.9)$$

where  $P_{amb}$  is the ambient pressure. As noted earlier, we neglect the effect of surfactants on the downstream fluid interface. Therefore, surface tension there remains constant, resulting in (2.8) and (2.9).

To remove the stress singularity that would arise by applying the no-slip boundary condition at the DCL, a Navier slip boundary condition is applied along the moving substrate (Huh & Scriven 1971; Dussan 1976; Chan *et al.* 2013; Sibley, Nold & Kalliadasis 2015):

$$\mathbf{t}_s \cdot (\mathbf{v} - \mathbf{U}) = \lambda[\mathbf{n}_s \cdot \mathbf{T} \cdot \mathbf{t}_s], \quad (2.10)$$

where  $\lambda$  is the dimensionless slip length defined earlier. Symbols  $\mathbf{n}_s$ ,  $\mathbf{t}_s$  and  $\mathbf{U}$  correspond to the substrate’s normal, tangent and velocity vectors, respectively. This slip boundary condition is applied along the entire bottom substrate and is able to recover the no-slip condition ( $\mathbf{v} \rightarrow \mathbf{U}$ ) for distances greater than  $l_{slip}$  away from the DCL. Although the slip length will in general have different values in the advancing and receding phases, for simplicity we assume here that it has the same value in both phases. This assumption has worked well in our previous work on the parallel-plate system (Vandre *et al.* 2012, 2013, 2014). Note that, in the vertical direction, the no-penetration condition is applied to the bottom boundary.

In the hydrodynamic model, the microscopic contact angle  $\theta_{mic}$  serves as a boundary condition at the DCL to determine the free-surface shape (Blake 2006; Snoeijer & Andreotti 2013). In general,  $\theta_{mic}$  may depend on problem parameters such as the substrate speed, curtain height and feed flow rate (Kistler 1993; Shikhmurzaev 1997; Sui *et al.* 2014; Blake *et al.* 2015) (see § 1.1). Since we wish to isolate the influence of air stresses, we take the simplest view and assume  $\theta_{mic}$  to be equal to the static contact angle  $\theta_s$  (a fixed value) (Lowndes 1980; Eggers 2005; Vandre *et al.* 2013; Sui *et al.* 2014).

## 2.2. Surfactant transport

A steady convection–diffusion equation describes insoluble surfactant transport along the upstream fluid interface:

$$\nabla_s \cdot (\mathbf{v}_s \Gamma) = \frac{1}{Pe} \nabla_s^2 \Gamma, \quad (2.11)$$

where  $\nabla_s$  is the surface gradient operator and  $\mathbf{v}_s$  is the interface velocity. The surface Péclet number  $Pe = V_w/D_s$  is defined using the surface diffusion coefficient  $D_s$ . The dimensionless surfactant concentration  $\Gamma$  is scaled with  $K\Gamma_m$ , where  $K$  represents a scaling factor ( $K \gg 1$ ) and  $\Gamma_m$  is the mean surfactant concentration at the fluid interface. Because the flow along the interface carries surfactant towards the DCL, large concentration gradients arise there that are computationally prohibitive to resolve if we scale  $\Gamma$  with  $\Gamma_m$  only (i.e.  $K = 1$ ). As a result, we introduce a scaling factor  $K$  and choose  $K = 500$ .

The surfactant transport equation (2.11) is coupled with the tangential stress balance (2.6) through an equation of state (Schunk & Scriven 1997). For simplicity, we assume that the surfactant concentration is dilute enough to apply a linear equation of state (Ramé 2001; Campana *et al.* 2004; Kumar & Matar 2004; Campana *et al.* 2011):

$$\sigma = 1 - \Gamma. \tag{2.12}$$

Here, surface tension  $\sigma$  has been non-dimensionalized using the relation  $\sigma' = \sigma_m + (\sigma_o - \sigma_m)\sigma$ , where  $\sigma'$  represents the dimensional surface tension (Craster & Matar 2009).

We assume that surfactants do not deposit onto the solid surfaces. As a result, no-flux boundary conditions  $\mathbf{n} \cdot \nabla \Gamma = 0$  are applied at the DCL and also the upstream tip of the slot die (figure 2). These boundary conditions require that a constraint of constant surfactant mass be applied:

$$\int_S \Gamma \, ds = (1/K)S, \tag{2.13}$$

where  $S$  represents the total arclength of upstream fluid interface. Note that  $1/K$  in (2.13) results from scaling concentration by  $K\Gamma_m$ .

Surfactants can potentially influence the microscopic contact angle  $\theta_{mic}$  and induce surface-tension gradients at the same time. To isolate the influence of Marangoni stresses on wetting failure, we assume that  $\theta_{mic}$  is neutral at the DCL (i.e.  $\theta_{mic} = 90^\circ$ ) and remains unchanged by surfactants. In addition, when comparing curtain coating in the absence and presence of surfactants, the mean surface tensions  $\sigma_m$  are kept the same.

### 2.3. Solution method

The Navier–Stokes equations (2.1a,b), 1D description of the receding air flow (2.2), surfactant transport equation (2.11) and associated boundary and integral conditions (2.4)–(2.10), (2.12) and (2.13) are solved with the Galerkin finite element method. The liquid domain is partitioned into seven quadrangular regions and the air flow is only discretized in the 1D region (8) near the DCL (figure 3a). Regions (8) and (9) represent the 1D domain on which surfactant transport along the upstream fluid interface is solved.

To solve the free-boundary problem, the physical domain (figure 3a) is mapped to a computational domain whose coordinates are  $\eta$  and  $\xi$  (figure 3b). The mapping function satisfies the elliptic mesh generation equations (Carvalho & Scriven 1997; Nam & Carvalho 2009). Biquadratic basis functions are used for position and velocity variables, and linear discontinuous basis functions are used for pressure in the liquid phase. The air pressure and the surfactant concentration are also described by biquadratic basis functions.

We found that mesh quality is best when the contact-line position  $x_{DCL}$  (figure 3a) is located directly underneath the upstream tip of the slot die ( $x_{DCL} = 0$ ). When

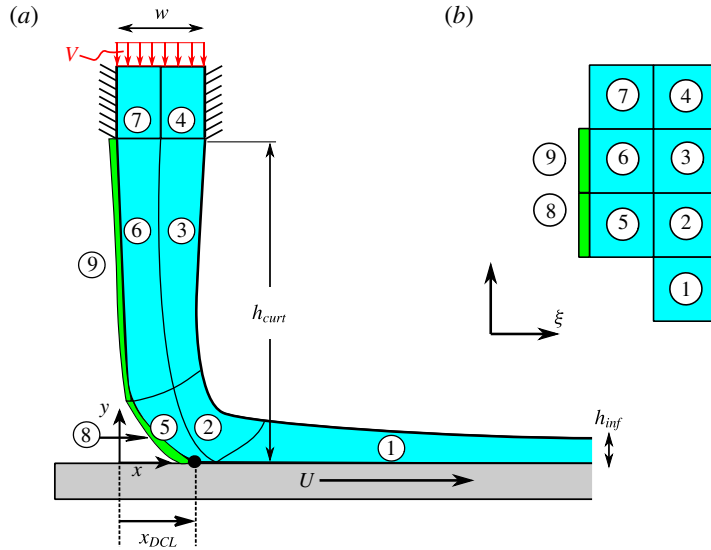


FIGURE 3. (Colour online) Schematics of (a) the physical coating domain and (b) the computational domain composed of seven liquid regions (1)–(7), air region (8) and surfactant transport regions (8) and (9).

the DCL moves downstream ( $x_{DCL} > 0$ ), elements near the DCL are stretched as the curtain is pulled (appendix A). In contrast, when  $x_{DCL} < 0$ , elements are stretched both near the DCL and near the upstream interface, where the curtain contacts a liquid heel that forms (appendix A). These mesh distortions make it very difficult to obtain discretization-independent steady-state solutions as the substrate speed  $U$  increases (at a fixed feed flow velocity  $V$ ). To mitigate this numerical issue, we fix  $x_{DCL}$  (as a flow parameter) and calculate  $V$  (as a dependent variable) as we trace solution paths to higher substrate speeds  $U$  (using first-order continuation). As expected,  $V$  must increase as  $U$  increases to hold the DCL position fixed (appendix B).

Since the interface bends sharply near the DCL (figure 3a), a larger number of elements near the DCL is required to resolve large gradients in the interface curvature. These gradients become larger as  $Ca$  increases. As a consequence, we found that element sizes near the DCL need to be less than  $10^{-3}l_{slip}$  to obtain mesh-independent solutions. Convergence is tested by systematically varying the number of elements to verify that solutions are mesh-independent (i.e. less than 2% variation in  $Ca^{crit}$  predicted from solution paths in § 3).

#### 2.4. Model parameters

Because we are most interested in how flow behaviour changes as the substrate speed increases for fixed fluid properties, it is convenient to choose a representative set of dimensional parameters. Motivated by experimental data, we take  $\mu_{adv} = 25$  cP,  $\mu_{rec} = 0.018$  cP,  $\sigma = 70$  mN m $^{-1}$  and  $\rho = 1000$  kg m $^{-3}$ . In addition, since we would like to isolate the effects of substrate speed and feed flow rate, we assume a neutral microscopic contact angle of  $\theta_{mic} = 90^\circ$ . We note that, even for this value of  $\theta_{mic}$ , predictions of the hybrid model for the parallel-plate geometry are in excellent agreement with results from a model that uses a full 2D description of both the air

and liquid phases (Liu *et al.* 2016). For this reason, we expect that a 1D description of the air flow is sufficient for accurately describing the behaviour of curtain coating.

To avoid the prohibitive computational costs that come with having too large a flow domain, we fix the curtain height at  $h_{\text{curr}} = 1$  cm. Although this is smaller than typical curtain heights ( $\sim 2\text{--}25$  cm), we expect that the results reported here will show the same qualitative behaviour as results for larger curtain heights.

Since smaller values of the slip length mean more elements near the DCL and a higher computational cost, a relatively large slip length  $l_{\text{slip}} = 10^{-5}$  m is selected for numerical convenience. Other runs we have performed (not shown here) and our previous work with the parallel-plate geometry (Liu *et al.* 2016) indicate that an increase in the slip length only increases the  $Ca^{\text{crit}}$  values without changing the qualitative nature of the solutions. We note that our choice of  $l_{\text{slip}}$  leads to a situation where the slip length is larger than the thickness of the air film. However, this was also the case in our previous work on the parallel-plate system (Vandre *et al.* 2013), yet the hydrodynamic model yielded predictions consistent with key experimental observations. This suggests that slip in the air phase, while necessary to include, may not play a dominant role in determining the main aspects of dynamic wetting failure for the flows considered in Vandre *et al.* (2013).

We consider values of  $U$  (substrate speed) from  $\sim 0.1$  to  $10$  m s $^{-1}$  and  $V$  (feed flow velocity) from  $\sim 0.1$  to  $1$  m s $^{-1}$ , and take the slot width  $w$  to be  $1$  mm. With the parameter choices listed above, this yields values of  $h_{\text{inf}}$  from  $\sim 0.1$  to  $1$  mm (appendix B). In addition,  $Ca$  varies from  $\sim 0.1$  to  $2.5$ ,  $Re$  varies from  $\sim 1$  to  $40$ ,  $Bo$  varies from  $\sim 10^{-3}$  to  $10^{-1}$ , and the dimensionless slip length  $\lambda$  varies from  $\sim 10^{-2}$  to  $10^{-1}$ . Note that, since the liquid properties are fixed,  $Ca$ ,  $Re$ ,  $Bo$  and  $\lambda$  change as the substrate speed and feed flow velocity are varied.

### 3. Influence of receding phase and comparison with parallel-plate system

In this section, the influence of the receding phase on wetting failure in curtain coating is studied. A comparison of the critical capillary number  $Ca^{\text{crit}}$  is also made between curtain coating and the parallel-plate system examined in our previous work (Vandre *et al.* 2012, 2013, 2014; Liu *et al.* 2016) (figure 1*b*) to demonstrate the influence of the curtain flow on the onset of wetting failure.

The macroscopic contact angles  $\theta_M$  (figure 2) are determined as a function of the capillary number  $Ca$  to construct steady-state solution paths (figure 4*a*). Solution paths are computed for zero and non-zero viscosity ratios  $\chi = \mu_{\text{rec}}/\mu_{\text{adv}}$  in curtain coating to demonstrate the influence of the viscosity in the receding phase  $\mu_{\text{rec}}$ .

For  $\chi > 0$  ( $\chi = 10^{-2}$ , blue squares, and  $7.2 \times 10^{-4}$ , black diamonds),  $\theta_M$  increases with  $Ca$  until reaching a limit point at a critical capillary number  $Ca^{\text{crit}}$  (figure 4*a*). Beyond this  $Ca^{\text{crit}}$  value ( $Ca > Ca^{\text{crit}}$ ), we are unable to find any 2D steady-state solutions. We assume that this corresponds to the point where the system develops 3D or transient flows resulting in wetting failure (Ledesma-Aguilar, Hernandez-Machado & Pagonabarraga 2013; Vandre *et al.* 2013). However, if the receding air is not accounted for ( $\chi = 0$ , green circles), the system appears to maintain steady 2D wetting with  $\theta_M \rightarrow 180^\circ$  as the substrate speed approaches infinity ( $Ca \rightarrow \infty$ ). Similar behaviour is also predicted in fluid displacement between parallel plates (Vandre *et al.* 2013) and in plunge coating (Benkreira & Khan 2008; Benkreira & Ikin 2010).

Figure 4*a*) clearly demonstrates the influence of the receding flow on the  $Ca^{\text{crit}}$  values. With a high-viscosity receding gas ( $\chi = 10^{-2}$ ), the system tends to have wetting failure at a smaller substrate speed, which is consistent with prior studies

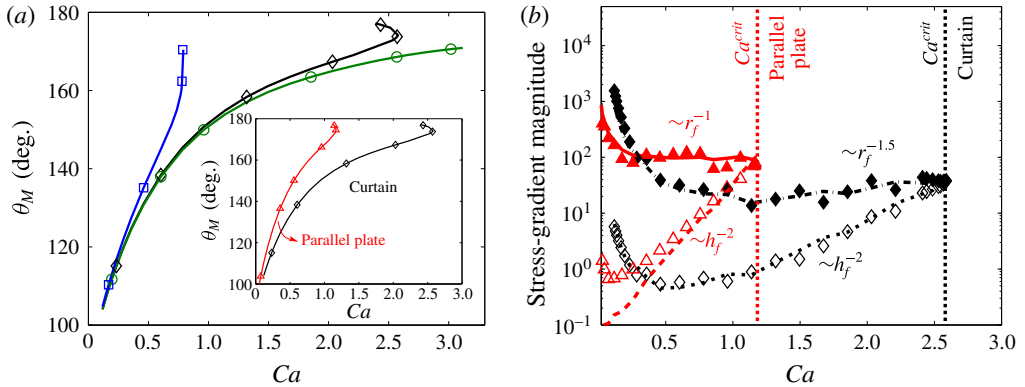


FIGURE 4. (Colour online) (a) Solution paths for various viscosity ratio  $\chi$  values,  $\chi = 10^{-2}$  (blue squares),  $\chi = 7.2 \times 10^{-4}$  (black diamonds) and  $\chi = 0$  (green circles), in curtain coating. Inset: solution paths for  $\chi = 7.2 \times 10^{-4}$  in curtain coating (black diamonds) and the parallel-plate system (red triangles). (b) Magnitude of stress gradients at the interface IP for curtain coating (black diamonds) and the parallel-plate system (red triangles) for  $\chi = 7.2 \times 10^{-4}$ . The capillary-stress gradients (filled symbols) match the air-pressure gradients (open symbols) at  $Ca^{crit}$  values denoted by dotted lines. Values of other parameters are  $x_{DCL} = 0$  and  $\theta_{mic} = 90^\circ$ . For the parallel-plate system, the scaled slip length  $\lambda = 10^{-2}$ . For curtain coating when  $\chi = 7.2 \times 10^{-4}$ ,  $\lambda$  varies from 0.0096 to 0.095 as  $Ca$  increases.

in parallel-plate geometries (Sbragaglia *et al.* 2008; Chan *et al.* 2013; Vandre 2013; Vandre *et al.* 2013). However, the onset of wetting failure is completely missed when neglecting stress contributions from the receding phase ( $\chi = 0$ ). Therefore, it is crucial to incorporate the stresses from the receding phase to even predict the onset of wetting failure in curtain coating. Although curtain coating has been studied in previous work (Kistler 1985; Miyamoto & Katagiri 1997; Wilson *et al.* 2006; Lukyanov & Shikhmurzaev 2007; Decent 2008), to the best of the authors' knowledge this is the first work that predicts the onset of wetting failure in this important flow.

As mentioned in § 1.2, the flows in curtain coating and the parallel-plate system are significantly different. The main difference lies in the impinging liquid curtain, which may lead to high hydrodynamic pressure near the DCL (figure 1). The inset of figure 4(a) demonstrates the influence of the liquid curtain on  $Ca^{crit}$  and  $\theta_M$ . At this particular set of conditions, the critical capillary number in curtain coating is almost twice that obtained in the parallel-plate system. (Inertial and gravitational effects are neglected in the parallel-plate system. For curtain coating,  $Re = 30.37$  and  $Bo = 1.54 \times 10^{-3}$  at  $Ca = Ca^{crit}$ .)

This delay in the onset of wetting failure in curtain coating agrees with prior experimental observations: by manipulating the flow in curtain coating, the critical coating speed (i.e. air entrainment) is delayed and the dynamic contact angles are reduced in comparison with plunge coating (Blake *et al.* 1994, 1999, 2004; Yamamura 2007). The term ‘hydrodynamic assist’ is used to describe the delay of air entrainment caused by manipulation of the flow (§ 1.1) (Blake *et al.* 1994). In § 4, we will propose a physical explanation of hydrodynamic assist by using a stress-gradient analysis near the DCL.

Although the values of the dimensionless slip lengths are comparable in the two systems, their definitions are not the same (one is scaled by the gap width  $H$  between the two plates (figure 1) and the other is scaled by  $Q/U$ ). Therefore, to study the mechanism of hydrodynamic assist, the analysis in §4 will only focus on curtain coating.

In prior work on wetting failure in the parallel-plate geometry, we proposed that wetting failure occurs when capillary-stress gradients can no longer provide the pressure gradient required to pump the receding fluid away from the DCL (Vandre *et al.* 2013). To examine whether this wetting failure mechanism is still valid in curtain coating, capillary-stress gradients (filled symbols) and air-pressure gradients (open symbols) at the interface IP in curtain coating (black diamonds) and the parallel-plate system (red triangles) are plotted as a function of  $Ca$  in figure 4(b). The critical capillary number  $Ca^{crit}$  in each system corresponds to the flow condition where the capillary-stress and air-pressure gradients match, indicating that the physical mechanisms that govern wetting failure in both systems are similar despite the significant difference in geometry and flow fields. Note that the pressure gradient in the receding phase grows faster than the capillary-stress gradient as  $Ca$  increases, thereby imposing a limitation to dynamic wetting.

Use of lubrication theory and the slip boundary condition yields the prediction that the magnitude of the capillary-stress gradient  $\sim r_f^{-1}$ , where  $r_f$  is the distance to the IP (figure 2) (Vandre *et al.* 2013; Liu *et al.* 2016). This scaling is obeyed by the data from the parallel-plate system, but the data from curtain coating show a stronger dependence on the IP location ( $\sim r_f^{-1.5}$ ) (figure 4b). In both systems, the air-pressure gradient  $\sim h_f^{-2}$  (figure 4b), where  $h_f$  is the IP height, consistent with lubrication theory (Vandre *et al.* 2013; Liu *et al.* 2016). The stronger dependence of the capillary-stress gradient on the IP location in curtain coating can be attributed to the hydrodynamic pressure exerted by the impinging curtain (see §4 for more details).

#### 4. Hydrodynamic assist in curtain coating

As mentioned in §1.1, hydrodynamic assist is the manipulation of curtain coating to assist dynamic wetting and delay the onset of wetting failure (i.e. air entrainment) (Blake *et al.* 1994; Miyamoto & Katagiri 1997). Prior experimental observations show that hydrodynamic assist is sensitive to the DCL position  $x_{DCL}$  (Blake *et al.* 1994; Clarke 1995; Blake *et al.* 1999; Yamamura *et al.* 2000; Blake *et al.* 2004; Marston, Decent & Simmons 2006; Chang *et al.* 2012). In this section, we first show the flow fields for different  $x_{DCL}$  and connect these with prior experimental observations (Blake *et al.* 1994; Clarke 1995; Marston *et al.* 2006; Chang *et al.* 2012). We then propose a physical mechanism for hydrodynamic assist based on these flow fields and a stress-gradient analysis.

##### 4.1. Flow fields with different $x_{DCL}$

Air/liquid displacement ( $\chi = 7.2 \times 10^{-4}$ ) in curtain coating is studied at various positions of  $x_{DCL}$ , which is controlled by the feed flow velocity  $V$  in experiments at fixed substrate speed  $U$  and curtain height  $h_{curt}$  (Blake *et al.* 1994; Miyamoto & Katagiri 1997; Marston *et al.* 2007; Chang *et al.* 2012). Decreasing  $V$  allows the substrate to drag the DCL downstream, whereas increasing  $V$  tends to move the DCL upstream.

Figure 5 shows (a–c) pressure contours and (d–f) velocity-magnitude contours for three flow configurations (corresponding to three  $x_{DCL}$  values) in curtain coating

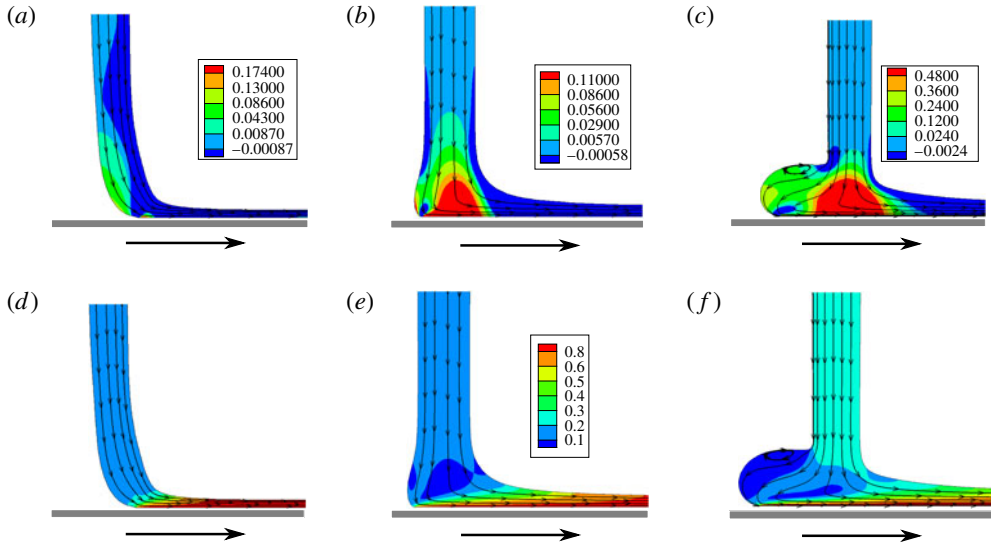


FIGURE 5. (Colour online) (a–c) Pressure contours and (d–f) velocity-magnitude contours for various  $x_{DCL}$  values:  $x_{DCL} = 1$  (a,d),  $x_{DCL} = 0$  (b,e) and  $x_{DCL} = -1$  (c,f). Values of other parameters are viscosity ratio  $\chi = 7.2 \times 10^{-4}$  and  $\theta_{mic} = 90^\circ$ . Here,  $Ca = 1.33$  ( $x_{DCL} = 1$ ),  $2.59$  ( $x_{DCL} = 0$ ) and  $1.36$  ( $x_{DCL} = -1$ ). Note that  $Ca = Ca^{crit}$  except for the case  $x_{DCL} = -1$ . In addition,  $Re = 11.99$  ( $x_{DCL} = 1$ ),  $30.37$  ( $x_{DCL} = 0$ ) and  $34.93$  ( $x_{DCL} = -1$ ), and  $Bo = 9.12 \times 10^{-4}$  ( $x_{DCL} = 1$ ),  $1.54 \times 10^{-3}$  ( $x_{DCL} = 0$ ) and  $7.33 \times 10^{-3}$  ( $x_{DCL} = -1$ ).

(Blake *et al.* 1994; Clarke 1995; Miyamoto & Katagiri 1997; Marston *et al.* 2006; Chang *et al.* 2012): (a,d) bead pulling,  $x_{DCL} > 0$ ; (b,e) DCL right beneath the liquid curtain,  $x_{DCL} = 0$ ; and (c,f) heel formation,  $x_{DCL} < 0$ . Because it is easiest to compare different cases when the spatial scales are the same, all lengths have been rescaled by the slot width  $w$  in this plot and subsequent ones. Note that the first two cases are at their respective critical capillary numbers  $Ca^{crit}$ , whereas the last one is not. This is because, in the last case, mesh distortion is so strong that it prevents us from obtaining converged solutions before  $Ca^{crit}$  can be clearly identified. Impinging liquid pressurizes the flow underneath the curtain, with the effect being most prominent when the DCL is right beneath the liquid curtain and in the heel-formation configuration. The effect is not as prominent in the bead-pulling configuration since the curtain is dragged by the substrate.

Prior experimental observations suggest that hydrodynamic assist is most influential (i.e. the substrate speed  $U^{crit}$  is maximum) when the contact line is right beneath the liquid curtain (Blake *et al.* 1994, 1999; Yamamura *et al.* 2000; Wilson *et al.* 2006). Our results show that, when  $x_{DCL} = 0$ ,  $Ca^{crit}$  is the largest and its value is almost twice that when  $x_{DCL} = 1$  (figure 5a,b). The degree of hydrodynamic assist is related to the distance between the DCL and the curtain impingement position (i.e. right beneath the upstream tip of the slot die) (figure 5a–c). Hydrodynamic pressure due to the inertia of the liquid curtain has the strongest effect when the impingement position overlaps the DCL (i.e.  $x_{DCL} = 0$ ) because dynamic wetting and wetting failure take place at the DCL (i.e. air bubbles break off vertices of the sawtooth-shaped DCL) (Blake & Ruschak 1979; Vandre *et al.* 2014).

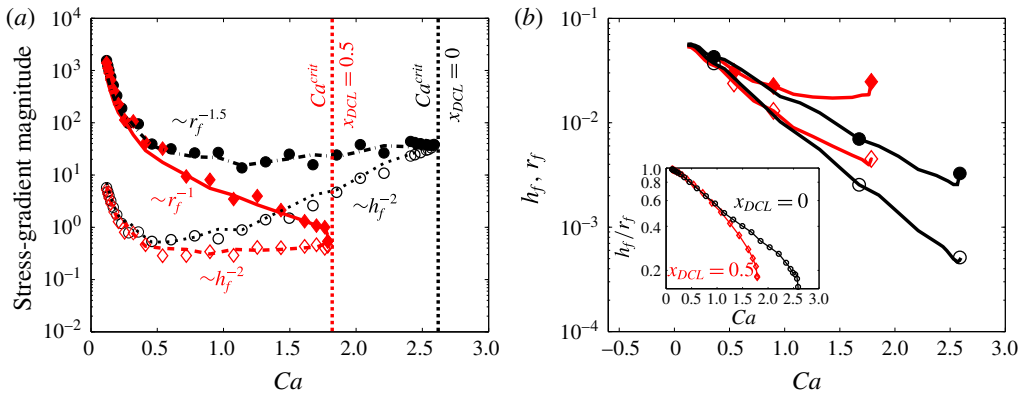


FIGURE 6. (Colour online) (a) Magnitude of capillary-stress (filled symbols) and air-pressure (open symbols) gradients at the IP for  $x_{DCL} = 0$  (black circles) and  $x_{DCL} = 0.5$  (red diamonds). (b) IP radial distance  $r_f$  (filled symbols) and height  $h_f$  (open symbols) as a function of  $Ca$  for  $x_{DCL} = 0$  (black circles) and  $x_{DCL} = 0.5$  (red diamonds). Inset: the ratio between the two length scales for  $x_{DCL} = 0$  (black circles) and  $x_{DCL} = 0.5$  (red diamonds). Values of other parameters are viscosity ratio  $\chi = 7.2 \times 10^{-4}$  and  $\theta_{mic} = 90^\circ$ .

In contrast, in the bead-pulling configuration, the effect of hydrodynamic assist is weakened because the high-pressure region is not as prominent and the DCL is away from the impingement position (figure 5a). In the heel-formation configuration, although hydrodynamic pressure is enhanced under the curtain, the increased distance between the impingement position and the DCL results in weak hydrodynamic assist (figure 5c).

In all the flow configurations, liquid must accelerate near the DCL to match the substrate velocity (figure 5d–f). Consequently, liquid pressure decreases sharply near the DCL, providing a pressure gradient that draws liquid towards the moving substrate (figure 5a–c). The low-pressure zone paired with the high-pressure region under the curtain allow the  $x_{DCL} = 0$  case to achieve high coating speeds (figure 5b). In the heel-formation configuration, however, the high pressure under the curtain is located far from the DCL and directs liquid upstream (figure 5c). This results in a recirculation region (figure 5f), similar to what is observed experimentally (Clarke & Stattersfield 2006).

#### 4.2. Mechanism of hydrodynamic assist

As noted in §3, the mechanism of wetting failure is similar in curtain coating and the parallel-plate system. Here, we investigate the influence of hydrodynamic assist on the wetting failure mechanism. Figure 6(a) shows the capillary-stress gradient (filled symbols) and air-pressure gradient (open symbols) at the interface IP as a function of  $Ca$  for  $x_{DCL} = 0$  (black circles) and  $x_{DCL} = 0.5$  (red diamonds). Notably, when  $x_{DCL} = 0$  the capillary-stress gradient is larger and has a stronger dependence on the IP location ( $\sim r_f^{-1.5}$ ) in comparison with the case when  $x_{DCL} = 0.5$  ( $\sim r_f^{-1}$ ). We point out that the  $r_f^{-1}$  behaviour observed when  $x_{DCL} = 0.5$  is similar to that in the previously examined parallel-plate geometry (figure 4b). Therefore, the stronger dependence of the capillary-stress gradient on  $r_f$  when  $x_{DCL} = 0$  can be attributed to the presence of hydrodynamic assist.

Figure 6(b) shows the change of the interface IP height  $h_f$  (filled symbols) and radial distance  $r_f$  (open symbols) with  $Ca$  (see figure 2 for definitions of  $h_f$  and  $r_f$ ). For both  $x_{DCL} = 0$  (black circles) and  $x_{DCL} = 0.5$  (red diamonds), the IP migrates towards the DCL (i.e.  $h_f$  and  $r_f$  decreasing) as  $Ca$  increases because the interface curvature needs to increase to balance the increasing viscous stresses from the air. Notably, the IP for  $x_{DCL} = 0$  is closer to the DCL than that for  $x_{DCL} = 0.5$  as  $Ca$  approaches the onset of wetting failure, meaning that the interface curvature for  $x_{DCL} = 0$  is larger than that for  $x_{DCL} = 0.5$ . As a result, the capillary-stress gradient for  $x_{DCL} = 0$  is larger than that for  $x_{DCL} = 0.5$ , which is consistent with what is shown in figure 6(a).

The inset of figure 6(b) shows the ratio between  $h_f$  and  $r_f$  for  $x_{DCL} = 0$  and  $x_{DCL} = 0.5$ . This ratio is related to the angle of the wedge formed in the receding phase (figure 2); a larger ratio corresponds to a smaller macroscopic contact angle  $\theta_M$ . The inset of figure 6(b) shows that this ratio is larger when  $x_{DCL} = 0$ . This is a consequence of the strong hydrodynamic pressure near the DCL when  $x_{DCL} = 0$ , which suppresses the penetration of the air film. Therefore, the model results suggest that the macroscopic contact angle  $\theta_M$  in curtain coating is reduced by hydrodynamic assist, which is consistent with experimental observations that hydrodynamic assist leads to a reduction in the dynamic contact angle  $\theta_D$  (Blake *et al.* 1999, 2004; Clarke & Stattersfield 2006; Decent 2008). In § 5, we will discuss the influence of air stresses on the contact-angle behaviour.

Together, figures 5 and 6 suggest that hydrodynamic assist can be attributed to the strong pressure generated by the inertia of the impinging curtain. This pressure creates large gradients in the interface curvature near the DCL, which in turn enhances the capillary-stress gradient there and lowers the dynamic contact angle. These larger capillary-stress gradients more effectively pump air away from the DCL and delay the onset of wetting failure.

## 5. Variation of dynamic contact angle with feed flow rate

As mentioned in § 1.1, varying the feed flow rate  $Q = wV$  in curtain coating can delay the onset of wetting failure (i.e. increase the critical capillary number  $Ca^{crit}$ ). Flow visualizations show that the dynamic contact angle also varies with  $Q$  (Blake *et al.* 1994, 1999). In this section, we examine the influence of  $Q$  on  $Ca^{crit}$  and the macroscopic contact angle  $\theta_M$ . Because the Reynolds number  $Re = \rho Vw/\mu_{adv}$  is directly proportional to the feed flow velocity  $V$ , we use it as a proxy for the feed flow rate.

Steady-state solution paths for various values of  $x_{DCL}$  are shown in figure 7. As mentioned in § 2.3, we fix the value of  $x_{DCL}$  and calculate  $Re$  as we trace the solution paths to higher capillary numbers  $Ca$ . The results show that, at the largest  $Ca$  for each  $x_{DCL}$ , the corresponding  $Re$  (i.e. feed flow rate) increases as the DCL moves upstream (i.e. decreasing  $x_{DCL}$ ).

Owing to strong mesh distortion, the solution path for the heel-formation configuration ( $x_{DCL} = -1$ , asterisks in figure 7) does not reach a limit point and thus the corresponding  $Ca^{crit}$  cannot be computed. However, it is clear that, when  $x_{DCL} = -1$ , the macroscopic contact angles  $\theta_M$  are increased in comparison with  $x_{DCL} = 0$  (triangles), suggesting that wetting failure occurs at a smaller  $Ca^{crit}$ . Therefore, figure 7 implies that  $Ca^{crit}$  increases first and then decreases as the feed flow rate increases. To the best of the authors' knowledge, this is the first time the non-monotonic behaviour of  $Ca^{crit}$  (i.e. air entrainment) in curtain coating has been predicted.

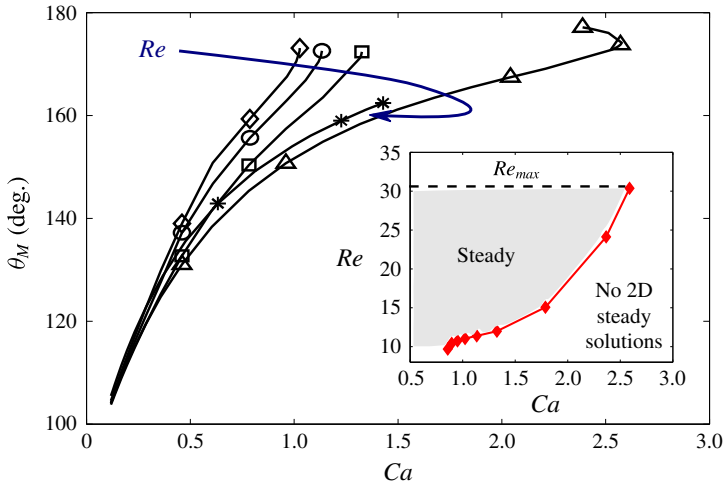


FIGURE 7. (Colour online) Solution paths for various  $x_{DCL}$  values (i.e. feed flow rates) when viscosity ratio  $\chi = 7.2 \times 10^{-4}$ :  $x_{DCL} = 3$  ( $Re = 11.04$ , diamonds),  $x_{DCL} = 2$  ( $Re = 11.39$ , circles),  $x_{DCL} = 1$  ( $Re = 11.99$ , squares),  $x_{DCL} = 0$  ( $Re = 30.37$ , triangles) and  $x_{DCL} = -1$  ( $Re = 34.93$ , asterisks). Note that the listed  $Re$  values are those for the largest  $Ca$  in the respective solution paths. Inset: coating window with  $Re_{max}$  corresponding to the flow condition where  $x_{DCL} = 0$ . Values of other parameters are  $\chi = 7.2 \times 10^{-4}$  and  $\theta_{mic} = 90^\circ$ . The corresponding values of  $Bo$  are  $1.30 \times 10^{-3}$ ,  $1.12 \times 10^{-3}$ ,  $9.12 \times 10^{-4}$ ,  $1.54 \times 10^{-3}$  and  $7.33 \times 10^{-3}$ .

Among the various cases shown in figure 7, the solution path for  $x_{DCL} = 0$  shows the maximum  $Ca^{crit}$ , which is similar to experimental observations that the maximum hydrodynamic assist occurs when the DCL is right beneath the curtain (Blake *et al.* 1994, 1999; Yamamura *et al.* 2000). Figure 7 also shows that, at a given  $Ca$ , increasing the feed flow rate leads to a non-monotonic behaviour of  $\theta_M$  (i.e. the angle decreases first, then increases), which has been predicted by Wilson *et al.* (2001, 2006) in simulations that do not account for the air phase and will be discussed further below.

A coating window can be predicted by our model, as shown in the inset of figure 7. Here,  $Re$  is plotted as a function of  $Ca$  to demonstrate the high-speed limit (i.e. air entrainment) in curtain coating. The shaded area represents a steady coating regime, where  $Re_{max}$  corresponds to flow conditions at the maximum  $Ca^{crit}$  ( $x_{DCL} = 0$ ). As  $Re$  increases,  $Ca^{crit}$  increases and the regime of steady coating (at a fixed  $Re$ ) enlarges, suggesting that inertia is essential in curtain coating for maintaining steady wetting at higher speeds. However, because critical capillary numbers could not be computed for  $Re > Re_{max}$  (associated with the heel-formation configurations,  $x_{DCL} < 0$ ), this plot only shows part of the coating window usually observed in experiments (Blake *et al.* 1999, 2004; Marston *et al.* 2006, 2007, 2009).

As noted in § 1.1, the predictions reported by Wilson *et al.* (2001, 2006) show that the reduction in the apparent contact angle (i.e. interface angle calculated 20  $\mu\text{m}$  from the DCL) is much smaller ( $< 10^\circ$ ) than that in dynamic contact angle  $\theta_D$  ( $\sim 20^\circ$ ) observed experimentally by Blake *et al.* (1999). Since their model does not consider the contribution of air stresses, here we investigate how the presence of air stresses influences the variation of  $\theta_M$  with feed flow rate.

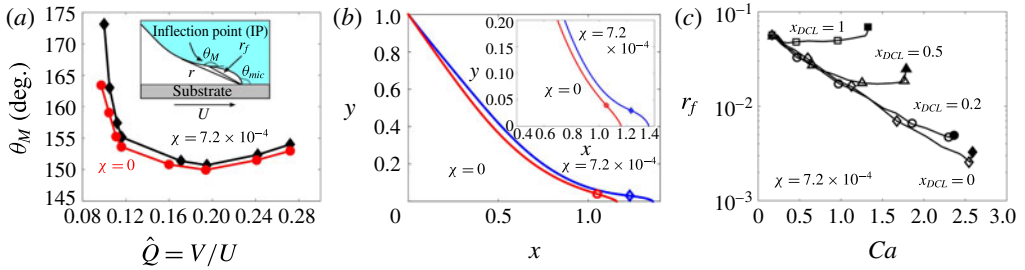


FIGURE 8. (Colour online) (a) Variation of macroscopic contact angles at the interface IP with  $\hat{Q}$  for viscosity ratio  $\chi = 7.2 \times 10^{-4}$  (diamonds) and  $\chi = 0$  (circles). (b) Interface profiles for  $\chi = 7.2 \times 10^{-4}$  (blue diamond) and  $\chi = 0$  (red circle) when  $\hat{Q} = 0.1$ . The DCL is at  $y = 0$  and symbols mark the IPs. Inset: interface profiles near  $y = 0$ . (c) IP radial distance  $r_f$  as a function of  $Ca$  for various  $x_{DCL}$  values when  $\chi = 7.2 \times 10^{-4}$ :  $x_{DCL} = 1$  (squares),  $x_{DCL} = 0.5$  (triangles),  $x_{DCL} = 0.2$  (circles) and  $x_{DCL} = 0$  (diamonds). Values of other parameters are  $\theta_{mic} = 90^\circ$  and  $Ca = 0.96$ .

The variation of macroscopic contact angle  $\theta_M$  with feed flow rate is shown in figure 8(a), where  $\theta_M$  is plotted as a function of  $\hat{Q} = V/U$  at  $Ca = 0.96$  (i.e. fixing substrate speed  $U$  and varying feed flow velocity  $V$ ). Curves of  $\theta_M$  in both air/liquid ( $\chi = 7.2 \times 10^{-4}$ , diamonds) and void/liquid ( $\chi = 0$ , circles) systems show a minimum corresponding to the smallest  $\theta_M$ . This trend is consistent with the non-monotonic behaviour of the dynamic contact angle  $\theta_D$  observed experimentally (Blake *et al.* 1999; Clarke & Stattersfield 2006).

Although the curtain height ( $h_{curt} = 1$  cm) in our model is not the same as that studied by Wilson *et al.* (2001, 2006) ( $h_{curt} = 3$  cm), the largest angle reduction predicted by our model in air/liquid displacement is around  $20^\circ$  (diamonds in figure 8a), which is very close to the experimental value reported by Blake *et al.* (1999) ( $\sim 20^\circ$ ). In contrast, the angle reduction in void/liquid displacement ( $\sim 15^\circ$ ) is smaller than that in air/liquid displacement. If we calculate an apparent contact angle at a distance of  $20 \mu\text{m}$  from the DCL as done by Wilson *et al.* (2001, 2006), the angle reductions are smaller and closer. For air/liquid displacement, it is  $\sim 8^\circ$ ; whereas for void/liquid displacement, it is  $\sim 7^\circ$ .

The larger reduction of  $\theta_M$  in air/liquid displacement suggests that the air phase plays a crucial role in curtain coating. This is because air stresses also contribute to determining the shape of the interface near the DCL (Chan *et al.* 2013; Vandre *et al.* 2013) and the value of  $\theta_M$ , especially near the onset of wetting failure (figure 4a). Figure 8(b) shows the influence of the receding-phase viscosity on the interface profile. At large scales, the interface profiles in the presence and absence of air look very similar, as illustrated in the main panel. At smaller scales, however, the inset shows that the air has a significant influence on interface shape. The interface IP is closer to the DCL and the interface is more elongated when the air viscosity is included.

The migration of the IP for various feed flow rates (i.e.  $x_{DCL}$ ) is shown in figure 8(c). The solid symbols in each curve represent the radial distance  $r_f$  of the IP (figure 2) at the respective  $Ca^{crit}$ . The IP for  $x_{DCL} = 0$  (diamonds) is closer to the DCL than those in other cases, consistent with a lower value of  $\theta_M$  (figure 7). As the DCL moves away from  $x_{DCL} = 0$  (i.e.  $x_{DCL} > 0$ ), the IP migration paths deviate from that for  $x_{DCL} = 0$  and stop at smaller  $Ca^{crit}$  values, consistent with higher values of  $\theta_M$ . In dimensional

terms, the radial distance to the IP at  $Ca = 0.96$  varies from  $\sim 18 \mu\text{m}$  for  $x_{DCL} = 0$  to  $\sim 50 \mu\text{m}$  for  $x_{DCL} = 1$ . These distances are comparable to what can be resolved experimentally.

Although the predicted  $Ca^{crit}$  values are of a similar order of magnitude as prior experiments ( $0.3 < Ca < 50$ ) (Blake *et al.* 1999, 2004; Marston *et al.* 2007), the difference in curtain height between our model and experimental set-ups prevents us from drawing more definitive conclusions. However, our results suggest that accounting for the air stresses near the DCL is necessary to properly describe the experimental observations reported by Blake *et al.* (1999).

## 6. Influence of insoluble surfactants on curtain coating

Motivated by the experiments of Marston *et al.* (2009) discussed in § 1.3, we examine here the influence of Marangoni stresses on wetting failure in curtain coating. Marston *et al.* (2009) observed that  $U^{crit}$  could be reduced by up to  $\sim 66.7\%$  upon the addition of surfactants, which corresponds to a reduction in  $Ca^{crit}$  of  $\sim 36\%$ . We examine here whether Marangoni stresses could be a possible mechanism for this.

Based on the parameters reported by Marston *et al.* (2009), we estimate that the Marangoni number  $M$  at the onset of wetting failure is  $O(1)$  or smaller, and the Péclet number  $Pe$  is  $O(10^5)$  (see definitions of  $M$  and  $Pe$  in § 2.2). Thus,  $M = 0.15$  and  $Pe = 10^3$  are chosen as representative Marangoni and Péclet numbers in our calculation. Based on our previous work in the parallel-plate geometry,  $Pe = 10^3$  is large enough to be in the convection-dominated limit (Liu *et al.* 2016).

### 6.1. Solution paths

The solution paths for different Marangoni numbers when  $x_{DCL} = 0$  are shown in figure 9. We choose to fix  $x_{DCL} = 0$  because this is where hydrodynamic assist is maximum, in both the presence and the absence of surfactants. The solution path for  $M = 0$  (circles) corresponds to the case where surfactants are absent (figure 7). Notably, the presence of Marangoni stresses ( $M > 0$ ) decreases  $Ca^{crit}$  and promotes the onset of wetting failure, suggesting a possible mechanism for the experimental observations of Marston *et al.* (2009). Figure 9 also demonstrates that increasing the strength of Marangoni stresses (i.e. higher  $M$  or surfactant concentration) will further decrease  $Ca^{crit}$ , which was also experimentally observed by Marston *et al.* (2009).

The inset of figure 9 shows the solution paths for  $M = 0$  and  $M = 0.15$  at  $x_{DCL} = 0.5$ . As noted in § 5, the feed flow rate at  $Ca^{crit}$  decreases as the DCL moves downstream. Therefore, the feed flow rates for solution paths in the inset of figure 9 are smaller than those leading to  $x_{DCL} = 0$  in figure 9. Notably, in going from  $x_{DCL} = 0$  to  $x_{DCL} = 0.5$ ,  $Ca^{crit}$  decreases 30% for the surfactant-free case (i.e.  $M = 0$ ). In contrast, the reduction in  $Ca^{crit}$  for  $M = 0.15$  is only 6.3%, suggesting that the influence of the feed flow rate on the critical substrate speeds (i.e. the degree of hydrodynamic assist) is weakened by Marangoni stresses. This decreased degree of hydrodynamic assist is similar to what is observed by Marston *et al.* (2009), again indicating that Marangoni stresses may play an important role in curtain coating.

### 6.2. Mechanism of influence of surfactants

Our previous work on the parallel-plate system (figure 1b) suggests that Marangoni stresses promote the onset of wetting failure by thinning the air film between the fluid interface and the substrate (Liu *et al.* 2016). However, since curtain coating has

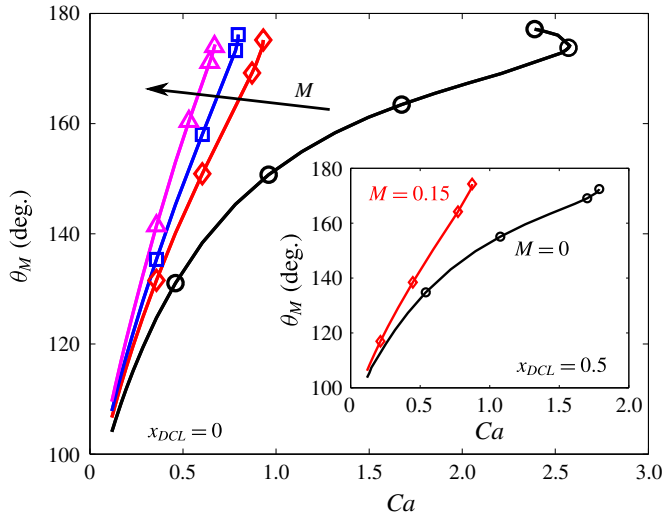


FIGURE 9. (Colour online) Solution paths for various  $M$  when  $x_{DCL} = 0$ :  $M = 0$  (black circles),  $M = 0.15$  (red diamonds),  $M = 0.3$  (blue squares) and  $M = 0.75$  (magenta triangles). Inset: solution paths for  $M = 0$  (black circles) and  $M = 0.15$  (red diamonds) when  $x_{DCL} = 0.5$ . Values of other parameters are viscosity ratio  $\chi = 7.2 \times 10^{-4}$  and  $\theta_{mic} = 90^\circ$ . For  $x_{DCL} = 0$ ,  $Re = 30.37$  and  $Bo = 1.54 \times 10^{-3}$  at  $Ca = Ca^{crit}$  when  $M = 0$ . For  $x_{DCL} = 0.5$ ,  $Re = 15.07$  and  $Bo = 7.94 \times 10^{-4}$  at  $Ca = Ca^{crit}$  when  $M = 0$ .

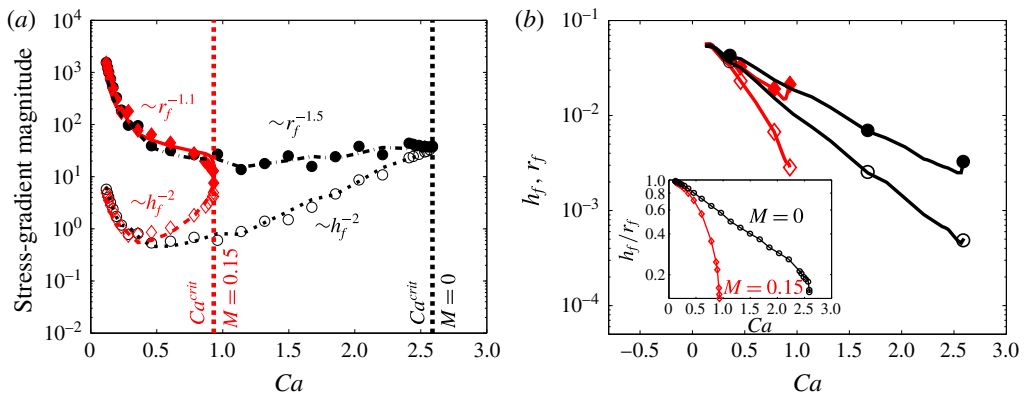


FIGURE 10. (Colour online) (a) Magnitude of stress gradients at the interface IP for  $M = 0$  (black circles) and  $M = 0.15$  (red diamonds). The capillary-stress gradients (filled symbols) match the air-pressure gradients (open symbols) at  $Ca^{crit}$  values denoted by dotted lines. (b) IP radial distance  $r_f$  (filled symbols) and height  $h_f$  (open symbols) as a function of  $Ca$  for  $M = 0$  (black circles) and  $M = 0.15$  (red diamonds). Inset: the ratio between the two length scales for  $M = 0$  (black circles) and  $M = 0.15$  (red diamonds). Values of other parameters are  $x_{DCL} = 0$ , viscosity ratio  $\chi = 7.2 \times 10^{-4}$  and  $\theta_{mic} = 90^\circ$ .

a significantly different geometry, it is not obvious that it shares the same physical mechanism. To address this issue, we perform a stress-gradient analysis.

Capillary-stress gradients (filled symbols) and air-pressure gradients (open symbols) at the interface IP are plotted as a function of  $Ca$  in figure 10(a) when Marangoni

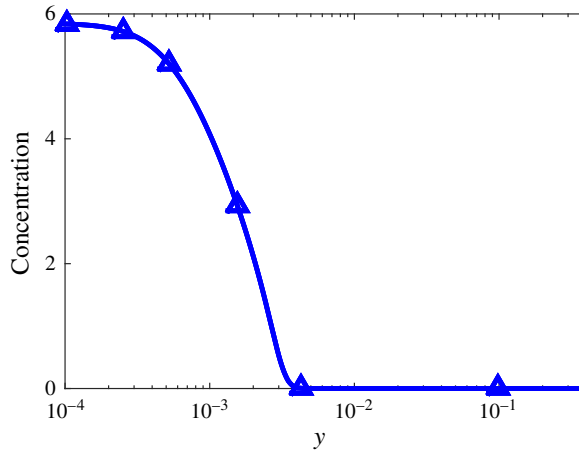


FIGURE 11. (Colour online) Surfactant concentration profile for  $M=0.15$  and  $Ca=0.93$ . The DCL is at  $y=0$ . Values of other parameters are  $x_{DCL}=0$ , viscosity ratio  $\chi=7.2 \times 10^{-4}$  and  $\theta_{mic}=90^\circ$ .

stresses are absent ( $M=0$ , black circles) and present ( $M=0.15$ , red diamonds). Similar to what we found in our previous work on the parallel-plate geometry (Liu *et al.* 2016), the presence of Marangoni stresses tends to increase the air-pressure gradient (red open diamonds) such that it matches the capillary-stress gradient (red filled diamonds) at a smaller  $Ca^{crit}$  compared to when  $M=0$ .

Flow along the interface carries surfactant towards the DCL, creating large concentration gradients there (figure 11). The surfactant concentration is largest near the DCL, leading to a Marangoni stress directed away from the DCL. Stronger shear stresses in the air phase are required to balance Marangoni stresses along the fluid interface (see (2.6)), and this requires air velocity changes over a smaller distance ( $du/dy$ ) near the DCL. Therefore, the air film near the DCL is thinned (i.e.  $h_f$  decreases), increasing the magnitude of the air-pressure gradient, which scales as  $h_f^{-2}$  (Vandre *et al.* 2013; Liu *et al.* 2016).

Figure 10(b) demonstrates the migration of the IP, where the characteristic length scales ( $r_f$ , filled symbols;  $h_f$ , open symbols) are plotted as a function of  $Ca$ . Notably, both  $r_f$  and  $h_f$  are smaller when  $M=0.15$  (diamonds) compared to when  $M=0$  (circles), indicating that the size of the air film shrinks in the presence of Marangoni stresses. Although smaller  $r_f$  values indicate a larger interface curvature and a stronger capillary-stress gradient, the decrease of  $h_f$  (with  $Ca$ ) when  $M=0.15$  is so drastic that the air-pressure gradient increases rapidly and becomes equal to the capillary-stress gradient at a smaller  $Ca$  than that when  $M=0$ .

The ratio between the two length scales ( $h_f/r_f$ ) for  $M=0$  (circles) and  $M=0.15$  (diamonds) is shown in the inset of figure 10(b). Owing to the large reduction in  $h_f$ , the ratio for  $M=0.15$  is much smaller than that for  $M=0$ . A smaller ratio corresponds to a larger macroscopic contact angle  $\theta_M$  at the IP (figure 2), which is consistent with the larger values of  $\theta_M$  in the solution paths when  $M>0$  (figure 9).

As discussed in §4, when Marangoni stresses are absent ( $M=0$ ), the strong dependence of the capillary-stress gradient on  $r_f$  when  $x_{DCL}=0$  can be attributed to the large pressure changes near the DCL ( $\sim r_f^{-1.5}$  in figure 10a). When Marangoni stresses are present ( $M=0.15$ ), figure 10(a) shows that the dependence of capillary-stress

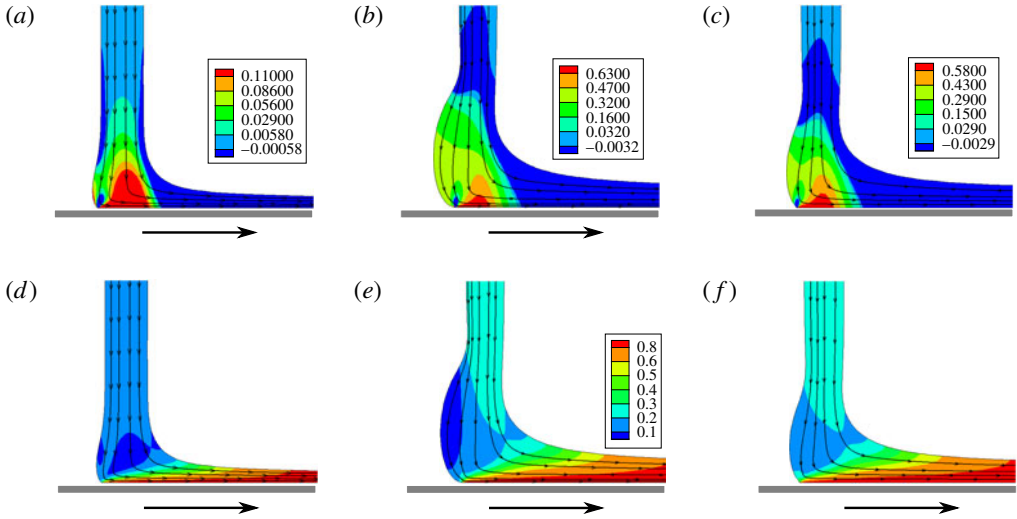


FIGURE 12. (Colour online) (a–c) Pressure contours and (d–f) velocity-magnitude contours for  $M=0$  (a,c,d,f) and  $M=0.15$  (b,e) at the onset of wetting failure. Values of other parameters are  $x_{DCL}=0$ , viscosity ratio  $\chi=7.2 \times 10^{-4}$  and  $\theta_{mic}=90^\circ$ . (a,d)  $Ca=2.59$ ,  $Re=30.37$  and  $Bo=1.54 \times 10^{-3}$ . (b,e)  $Ca=0.93$ ,  $Re=21.41$  and  $Bo=5.89 \times 10^{-3}$ . (c,f)  $Ca=0.96$ ,  $Re=20.94$  and  $Bo=5.3 \times 10^{-3}$ .

gradients on  $r_f$  is weakened ( $\sim r_f^{-1.1}$ ). To understand the reason for this, flow fields at the onset of wetting failure (i.e. at the respective  $Ca^{crit}$ ) for  $M=0$  and  $M=0.15$  are presented in figure 12.

Figure 12 shows (a–c) pressure contours and (d–f) velocity-magnitude contours for  $M=0$  and  $M=0.15$ . Panels (a,b) and (d,e) are at the onset of wetting failure, and we note that the value of  $Ca^{crit}$  when  $M=0$  is larger than that when  $M=0.15$ . Thus, panels (c,f) are for  $M=0$  at a value of  $Ca$  comparable to  $Ca^{crit}$  for  $M=0.15$ . In all cases,  $x_{DCL}=0$ .

When  $M=0$  (figure 12a,d), the curtain remains nearly perpendicular to the substrate and the impinging liquid pressurizes the flow underneath the curtain. In contrast, a liquid bulge is formed at the upstream fluid interface near the DCL when  $M=0.15$  (figure 12b,e). This liquid bulge results from the presence of Marangoni stresses, which counteract the impinging liquid and slow down the liquid velocity near the fluid interface and the DCL (figure 12e). We note that the bulge is not as prominent when  $M=0$  and  $Ca$  has a comparable value to  $Ca^{crit}$  for  $M=0.15$  (figure 12c,f). The low-speed region when  $M=0.15$  (figure 12e) indicates that inertial forces near the DCL are weakened, suggesting a weaker influence of the impinging liquid on the DCL compared to when  $M=0$ . This weakened influence may explain the weaker dependence of the capillary-stress gradient on  $r_f$  when  $M=0.15$  (figure 10a) and also the decrease in the degree of hydrodynamic assist observed by Marston *et al.* (2009).

Finally, we comment on several other phenomena that may be present in the experiments but are not accounted for in our calculations. First, the surfactants used in the experiments of Marston *et al.* (2009) were soluble, whereas our model assumes that the surfactants are insoluble. We expect that surfactant solubility will weaken Marangoni effects since surfactants could desorb from the fluid interface into the bulk.

Second, our model does not account for the possibility that surfactants may adsorb to the substrate. Third, the introduction of surfactants will lower the mean surface tension and the microscopic contact angle, which were taken as constant in the above calculations to isolate the influence of Marangoni stresses. Lowering  $\theta_{mic}$  would be expected to raise the value of  $Ca^{crit}$  since the substrate would be more wettable. As this is the opposite of what is observed in the experiments, it is not likely to be the cause of the decrease in  $Ca^{crit}$ . Accounting for these phenomena as well as larger curtain heights will be important to more fully understand the experimental observation that surfactants significantly promote the onset of wetting failure.

## 7. Conclusions

We have used a novel hybrid formulation of a hydrodynamic model to study dynamic wetting failure and hydrodynamic assist in curtain coating. The use of a 1D description of the air phase has allowed, for the first time, an examination of the influence of air stresses on this complicated coating flow. Indeed, without using a 1D description for the air phase, a full 2D description of the both the air and liquid phases would be computationally prohibitive.

Our model shows that inclusion of the air stresses is necessary to even predict the onset of wetting failure (§ 3). Once air stresses are included, our model is able to predict the non-monotonic behaviour of the critical capillary number with feed flow rate that has been observed experimentally (Blake *et al.* 1999) (§ 5). Inclusion of air stresses also leads to a larger variation of dynamic contact angle with feed flow rate, suggesting that accounting for air stresses is important to accurately describe experimental observations of the dynamic contact angle (Blake *et al.* 1999). In particular, our results raise the possibility that much of the behaviour observed in curtain-coating experiments can be qualitatively understood by accounting for air stresses and assuming a constant microscopic contact angle.

Our model also allows us to gain insight into the phenomenon of hydrodynamic assist (§ 4). Similar to what is observed experimentally, we find that the degree of hydrodynamic assist is largest when the DCL is right beneath the liquid curtain. The hydrodynamic pressure generated by the inertia of the impinging curtain leads to larger gradients in interface curvature near the DCL. These larger curvature gradients lead to stronger capillary-stress gradients that are more effective at pumping air away from the DCL, thus delaying the onset of wetting failure.

The influence of Marangoni stresses created by insoluble surfactants was also investigated, and we find that these stresses promote the onset of wetting failure and reduce the degree of hydrodynamic assist (§ 6). These findings are consistent with recent experimental observations (Marston *et al.* 2009) and suggest that Marangoni stresses are a possible mechanism. The Marangoni stresses thin the air film and increase the air-pressure gradients, making it more difficult for the capillary-stress gradients to pump the air away from the DCL.

Owing to computational limitations, some of the parameter values used in our model are quite different from those in experiments. Nevertheless, the model predictions are consistent with key experimental observations. We note that our assumption that the air can be described as a continuum in local thermodynamic equilibrium may break down as the air film becomes very thin (Sprittles 2015). It may also be important to account for slip at the air-liquid interface (Sprittles 2015). However, because the air film is long and slender, it may still be possible to describe its influence efficiently and accurately by using a 1D model.

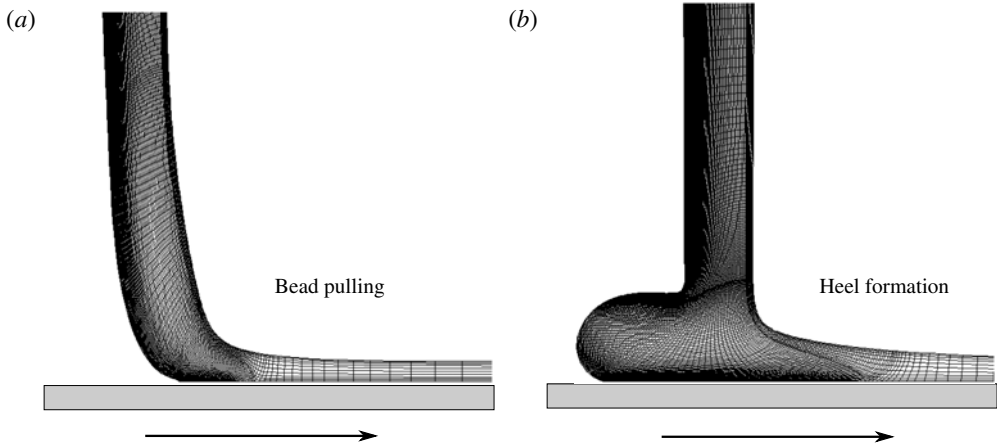


FIGURE 13. Mesh used in curtain coating for two flow configurations: (a) bead pulling and (b) heel formation.

The hybrid approach used here is limited principally by the degree to which the flow in the liquid phase can be resolved. Improvements in computational capacity will enable predictions of flows with parameters more representative of experimental setups (e.g. larger curtain heights), and thus allow for more quantitative comparisons with experimental data. If extended to 3D and transient flows, as well as to liquids with more complicated rheology, the hybrid approach may prove to be a computationally feasible way to accurately account for air stresses in these complex flows. Such an extension would be of interest not only for coating flows, but also for other problems in fluid mechanics such as rapid droplet spreading where there is a thin air layer near a DCL.

### Acknowledgement

This material is based upon work supported by the National Science Foundation under grant no. CBET-1434016.

### Appendix A. Finite element mesh

Figure 13 shows typical quadrilateral element meshes for two flow configurations: bead pulling (i.e.  $x_{DCL} > 0$ ) and heel formation (i.e.  $x_{DCL} < 0$ ). The highest concentration of elements is in the liquid domain near the DCL to resolve strong velocity and curvature gradients there. In the bead-pulling configuration, elements are stretched near the DCL. In contrast, in the heel-formation configuration, elements are stretched both near the DCL and near the transition between the falling curtain and the heel. For the same initial element arrangement, calculations do not converge in the heel-formation configuration when  $Ca \rightarrow Ca^{crit}$  because the mesh is strongly distorted. For this reason, we are not able to obtain  $Ca^{crit}$  values in the heel-formation configuration.

### Appendix B. Dimensional velocities and film thicknesses

As noted in § 2.3, we fix  $x_{DCL}$  as a flow parameter and calculate  $V$  (as a dependent variable) as we trace solution paths to higher  $U$ . As expected, the feed flow velocity

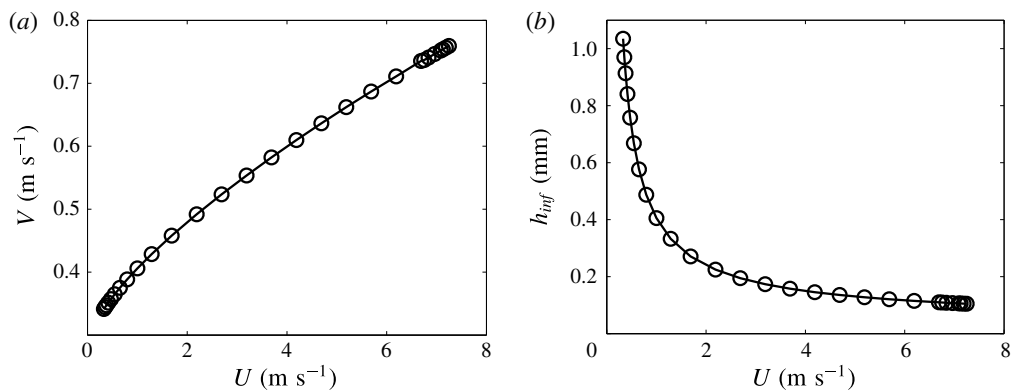


FIGURE 14. (a) Dependence of feed flow velocity  $V$  on substrate speed  $U$  in the absence of surfactants when  $x_{DCL} = 0$ . (b) Corresponding coating-film thickness  $h_{inf}$  from the balance of rates shown in panel (a). The parameters used for these calculations are given in § 2.4.

$V$  needs to increase as the substrate speed  $U$  increases to hold the DCL position fixed (figure 14a). However,  $V$  does not grow as fast as  $U$ , resulting in a decrease in coating-film thickness ( $h_{inf} = wV/U$ ) as  $U$  increases (figure 14b).

#### REFERENCES

- BENKREIRA, H. 2004 The effect of substrate roughness on air entrainment in dip coating. *Chem. Engng Sci.* **59** (13), 2745–2751.
- BENKREIRA, H. & IKIN, J. B. 2010 Dynamic wetting and gas viscosity effects. *Chem. Engng Sci.* **65** (5), 1790–1796.
- BENKREIRA, H. & KHAN, M. I. 2008 Air entrainment in dip coating under reduced air pressures. *Chem. Engng Sci.* **63** (2), 448–459.
- BLAKE, T. D. 2006 The physics of moving wetting lines. *J. Colloid Interface Sci.* **299** (1), 1–13.
- BLAKE, T. D., BRACKE, M. & SHIKHMURZAEV, Y. D. 1999 Experimental evidence of nonlocal hydrodynamic influence on the dynamic contact angle. *Phys. Fluids* **11** (8), 1995–2007.
- BLAKE, T. D., CLARKE, A. & RUSCHAK, K. J. 1994 Hydrodynamic assist of dynamic wetting. *AIChE J.* **40** (2), 229–242.
- BLAKE, T. D., DOBSON, R., BATTS, G. N. & HARRISON, W. J. 1995. Coating processes. US Patent 5391401.
- BLAKE, T. D., DOBSON, R. A. & RUSCHAK, K. J. 2004 Wetting at high Capillary numbers. *J. Colloid Interface Sci.* **279** (1), 198–205.
- BLAKE, T. D., FERNANDEZ-TOLEDANO, J.-C., DOYEN, G. & DE CONINCK, J. 2015 Forced wetting and hydrodynamic assist. *Phys. Fluids* **27** (11), 112101.
- BLAKE, T. D. & RUSCHAK, K. J. 1979 A maximum speed of wetting. *Nature* **282** (5738), 489–491.
- BROWN, D. R. 1961 A study of the behaviour of a thin sheet of moving liquid. *J. Fluid Mech.* **10** (2), 297–305.
- BURLEY, R. & KENNEDY, B. S. 1976 An experimental study of air entrainment at a solid/liquid/gas interface. *Chem. Engng Sci.* **31**, 901–911.
- CAMPANA, D. M., DI PAOLO, J. & SAITA, F. A. 2004 A 2-D model of Rayleigh instability in capillary tubes — surfactant effects. *Intl J. Multiphase Flow* **30**, 431–454.
- CAMPANA, D. M., UBAL, S., GIAVEDONI, M. D. & SAITA, F. A. 2011 A deeper insight into the dip coating process in the presence of insoluble surfactants: a numerical analysis. *Phys. Fluids* **23** (5), 052102.

- CARVALHO, M. S. & SCRIVEN, L. E. 1997 Flows in forward deformable roll coating gaps: comparison between spring and plane-strain models of roll cover. *J. Comput. Phys.* **138** (2), 449–479.
- CHAN, T. S., SRIVASTAVA, S., MARCHAND, A., ANDREOTTI, B., BIFERALE, L., TOSCHI, F. & SNOEIJER, J. H. 2013 Hydrodynamics of air entrainment by moving contact lines. *Phys. Fluids* **25** (7), 074105.
- CHANG, H.-K., SHIH, C.-J., LIU, T.-J. & TIU, C. 2012 Curtain coating of dilute suspensions. *Polym. Engng Sci.* **52** (1), 1–11.
- CHRISTODOULOU, K. N. & SCRIVEN, L. E. 1989 The fluid mechanics of slide coating. *J. Fluid Mech.* **208**, 321–354.
- CLARKE, A. 1995 The application of particle tracking velocimetry and flow visualization to curtain coating. *Chem. Engng Sci.* **50** (15), 2397–2407.
- CLARKE, A. & STATTERSFIELD, E. 2006 Direct evidence supporting nonlocal hydrodynamic influence on the dynamic contact angle. *Phys. Fluids* **18** (4), 048106.
- CRASTER, R. V. & MATAR, O. K. 2009 Dynamics and stability of thin liquid films. *Rev. Mod. Phys.* **81** (3), 1131–1198.
- DECENT, S. P. 2008 A simplified model of the onset of air entrainment in curtain coating at small Capillary number. *Chem. Engng Res. Des.* **86** (3), 311–323.
- DUSSAN, V. E. B. 1976 The moving contact line: the slip boundary condition. *J. Fluid Mech.* **77** (4), 665–684.
- EGGERS, J. 2005 Existence of receding and advancing contact lines. *Phys. Fluids* **17** (8), 082106.
- HUGHES, D. J. 1970 Method for simultaneously applying a plurality of coated layers by forming a stable multilayer free falling vertical curtain. US Patent 3508947.
- HUH, C. & SCRIVEN, L. E. 1971 Hydrodynamic model of steady movement of a solid/liquid/fluid contact line. *J. Colloid Interface Sci.* **35** (1), 85–101.
- JACQMIN, D. 2004 Onset of wetting failure in liquid–liquid systems. *J. Fluid Mech.* **517**, 209–228.
- KISTLER, S. F. 1985 The fluid mechanics of curtain coating and related viscous free surface flows with contact lines. PhD thesis, University of Minnesota.
- KISTLER, S. F. 1993 Hydrodynamics of wetting. In *Wettability* (ed. J. C. Berg), pp. 311–429. Marcel Dekker.
- KISTLER, S. F. & SCRIVEN, L. E. 1984 Coating flow theory by finite element and asymptotic analysis of the Navier–Stokes system. *Intl J. Numer. Meth. Fluids* **4**, 207–229.
- KUMAR, S. & MATAR, O. K. 2004 On the Faraday instability in a surfactant-covered liquid. *Phys. Fluids* **16** (1), 39–46.
- LEDESMA-AGUILAR, R., HERNANDEZ-MACHADO, A. & PAGONABARRAGA, I. 2013 Theory of wetting-induced fluid entrainment by advancing contact lines on dry surfaces. *Phys. Rev. Lett.* **110** (26), 264502.
- LIU, C.-Y., VANDRE, E., CARVALHO, M. S. & KUMAR, S. 2016 Dynamic wetting failure in surfactant solutions. *J. Fluid Mech.* **789**, 285–309.
- LOWNDES, J. 1980 The numerical simulation of the steady movement of a fluid meniscus in a capillary tube. *J. Fluid Mech.* **101** (3), 631–646.
- LUKYANOV, A. V. & SHIKHMURZAEV, Y. D. 2007 Effect of flow field and geometry on the dynamic contact angle. *Phys. Rev. E* **75** (5), 051604.
- MARCHAND, A., CHAN, T. S., SNOEIJER, J. H. & ANDREOTTI, B. 2012 Air entrainment by contact lines of a solid plate plunged into a viscous fluid. *Phys. Rev. Lett.* **108** (20), 204501.
- MARSTON, J. O., DECENT, S. P. & SIMMONS, M. J. H. 2006 Hysteresis and non-uniqueness in the speed of the onset of instability in curtain coating. *J. Fluid Mech.* **569**, 349–363.
- MARSTON, J. O., HAWKINS, V., DECENT, S. P. & SIMMONS, M. J. H. 2009 Influence of surfactant upon air entrainment hysteresis in curtain coating. *Exp. Fluids* **46**, 549–558.
- MARSTON, J. O., SIMMONS, M. J. H. & DECENT, S. P. 2007 Influence of viscosity and impingement speed on intense hydrodynamic assist in curtain coating. *Exp. Fluids* **42**, 483–488.
- MIYAMOTO, K. & KATAGIRI, Y. 1997 Curtain coating. In *Liquid Film Coating* (ed. S. Kistler & P. M. Schweizer), pp. 463–494. Chapman & Hall.

- NAM, J. & CARVALHO, M. S. 2009 Mid-gap invasion in two-layer slot coating. *J. Fluid Mech.* **631**, 397–417.
- RAMÉ, E. 2001 The spreading of surfactant-laden liquids with surfactant transfer through the contact line. *J. Fluid Mech.* **440**, 205–234.
- SBRAGAGLIA, M., SUGIYAMA, K. & BIFERALE, L. 2008 Wetting failure and contact line dynamics in a Couette flow. *J. Fluid Mech.* **614**, 471–493.
- SCHUNK, P. R. & SCRIVEN, L. E. 1997 Surfactant effects in coating processes. In *Liquid Film Coating* (ed. S. Kistler & P. M. Schweizer), pp. 495–536. Chapman & Hall.
- SCRIVEN, L. E. & STERNLING, C. V. 1960 The Marangoni effects. *Nature* **187**, 186–188.
- SHIKHMURZAEV, Y. D. 1997 Moving contact lines in liquid/liquid/solid systems. *J. Fluid Mech.* **334**, 211–249.
- SIBLEY, D. N., NOLD, A. & KALLIADASIS, S. 2015 The asymptotics of the moving contact line: cracking an old nut. *J. Fluid Mech.* **764**, 445–462.
- SNOEIJER, J. H. & ANDREOTTI, B. 2013 Moving contact lines: scales, regimes, and dynamical transitions. *Annu. Rev. Fluid Mech.* **45**, 269–292.
- SPRITTLES, J. E. 2015 Air entrainment in dynamic wetting: Knudsen effects and the influence of ambient air pressure. *J. Fluid Mech.* **769**, 444–481.
- SUI, Y., DING, H. & SPELT, P. D. 2014 Numerical simulations of flows with moving contact lines. *Annu. Rev. Fluid Mech.* **46**, 97–119.
- TRICOT, Y.-M. 1997 Surfactants: static and dynamic surface tension. In *Liquid Film Coating* (ed. S. Kistler & P. M. Schweizer), pp. 99–136. Chapman & Hall.
- VANDRE, E., CARVALHO, M. S. & KUMAR, S. 2012 Delaying the onset of dynamic wetting failure through meniscus confinement. *J. Fluid Mech.* **707**, 496–520.
- VANDRE, E., CARVALHO, M. S. & KUMAR, S. 2013 On the mechanism of wetting failure during fluid displacement along a moving substrate. *Phys. Fluids* **25** (10), 102103.
- VANDRE, E., CARVALHO, M. S. & KUMAR, S. 2014 Characteristics of air entrainment during dynamic wetting failure along a planar substrate. *J. Fluid Mech.* **747**, 119–140.
- VANDRE, E. A. 2013 Onset of dynamic wetting failure: the mechanics of high-speed fluid displacement. PhD thesis, University of Minnesota.
- WEINSTEIN, S. J. & RUSCHAK, K. J. 2004 Coating flows. *Annu. Rev. Fluid Mech.* **36** (1), 29–53.
- WILSON, M. C. T., SUMMERS, J. L., GASKELL, P. H. & SHIKHMURZAEV, Y. D. 2001 Moving contact-line model and the effect of hydrodynamic assist of dynamic wetting. In *IUTAM Symposium on Free Surface Flows* (ed. A. C. King & Y. D. Shikhmurzaev), pp. 345–352. Springer.
- WILSON, M. C. T., SUMMERS, J. L., SHIKHMURZAEV, Y. D., CLARKE, A. & BLAKE, T. D. 2006 Nonlocal hydrodynamic influence on the dynamic contact angle: slip models versus experiment. *Phys. Rev. E* **73** (4), 041606.
- YAMAMURA, M. 2007 Assisted dynamic wetting in liquid coatings. *Colloids Surf. A* **311**, 55–60.
- YAMAMURA, M., SUEMATSU, S., KAJIWARA, T. & ADACHI, K. 2000 Experimental investigation of air entrainment in a vertical liquid jet flowing down onto a rotating roll. *Chem. Engng Sci.* **55** (5), 931–942.